RESEARCH ARTICLE

Sub-regional design of the bionic bone scaffolds using macrostructural topology

Yangdong He[1,2†], Long Chao[1,2†], Chen Jiao[1,2], Hong Wang[1], Deqiao Xie[1], Guofeng Wu[3], Lin Wang[4], Changjiang Wang[5], Jianfeng Zhao[1,2*], Lida Shen[1,2*], and Huixin Liang[6,7*]

[1]Institute of Additive Manufacturing (3D Printing), Nanjing University of Aeronautics and Astronautics, Nanjing, 210016, China

[2]Jiangsu Key Laboratory of Digital Medical Equipment Technology, Nanjing University of Aeronautics and Astronautics, Nanjing, 210016, China

[3]Stomatological Digital Engineering Center, Nanjing Stomatological Hospital, Nanjing, 210008, China

[4]Nanjing Chamlion Laser Technology Co., Ltd, Nanjing, 210012, China

[5]Department of Engineering and Design, University of Sussex, Brighton, BN1 9RH, United Kingdom

[6]State Key Laboratory of Pharmaceutical Biotechnology, Division of Sports Medicine and Adult Reconstructive Surgery, Department of Orthopedic Surgery, Nanjing Drum Tower Hospital, The Affiliated Hospital of Nanjing University Medical School, Nanjing, 210008, China

[7]Jiangsu Engineering Research Center for 3D Bioprinting, Nanjing, 210008, China

†These authors contributed equally to this work.

*Corresponding authors:
Jianfeng Zhao
(zhaojf@nuaa.edu.cn)

Lida Shen
(ldshen@nuaa.edu.cn)

Huixin Liang
(hxliang@nuaa.edu.cn)

Abstract

With the increasing demand for bone repair, the bionic bone scaffolds have become a research hotspot. A sub-regional design method of the bionic bone scaffolds, using macrostructural topology, is proposed in this paper, aiming to provide a functionally enhanced region division method for the gradient design. The macrostructural topology was carried out by the bi-directional evolutionary structural optimization (BESO), dividing the predefined design domain into sub-region A and sub-region B. Subsequently, a combined probability sphere model and a distance-to-scale coefficient mapping model are established to implement the graded porosification based on the Voronoi tessellation. This approach takes geometric and mechanical continuity into fully account and assures a reasonable distribution of characteristic parameters, yielding to improve the mechanical strength under specific stress conditions. Finally, the scaffolds were fabricated by the laser powder bed fusion (LPBF) process using the Ti-6Al-4V powder. The results of compression tests are satisfactory, showing that the as-built specimens implement sub-regional functionality. The apparent elastic modulus and the ultimate strength range, respectively, between 1.50 GPa and 7.12 GPa (for the first module) and between 38.55 MPa and 268.03 MPa (for the second module), which conform to the required level of natural bone, providing a possibility for clinical application.

Keywords: Functionally graded porous materials; Bionic scaffolds; Bi-directional evolutionary structural optimization; Voronoi tessellation; Laser powder bed fusion

1. Introduction

With the acceleration of population aging and the frequent occurrence of traffic accidents, bone defect has become a hot issue in the field of bone tissue engineering. Since the self-healing cycle of natural bone takes a long time and its reconstruction ability is limited, appropriate artificial implants have become the primary choice[1]. Porous scaffold is the most common form of artificial implants. The introduction of porous features can reduce the apparent elastic modulus of artificial implants to a level close to that of a natural bone, yielding to reduces the phenomenon of stress shielding[2,3]. With the development of additive manufacturing technology, it is quite mature to realize the direct manufacturing of ultra-high precision porous scaffolds[4,5]. In order to unify the mechanical and biological properties of implants, Ti-6Al-4V scaffolds, fabricated by the laser powder bed fusion (LPBF) process, are one of the common artificial prostheses[6-9].

Human bone has a natural graded-pore distribution, allowing it to realize special functions at different gradient positions[10,11]. In the clinical environment, the porous scaffolds from previous studies cannot simulate the graded distribution of natural bone, leading to a mismatch in elastic modulus with the surrounding bone after implantation[12,13]; therefore, it will be losing the mechanical stability and the positive stress stimulation to primary bone tissue[14]. These losses will lead to osteoporosis and even atrophy, ending up with a failure to implant because of the looseness at the interface[15]. In order to simulate the graded distribution of a natural bone, an increasing number of researchers turn their attention to functionally graded porous materials (FGPMs)[16,17]. In bone tissue engineering, FGPMs mimic the gradient of the bone by controlling the nucleating points distribution of the porous scaffolds, or by setting the graded porosity[18]. Therefore, FGPMs have a more complex internal structure, which also puts forward higher requirements for researchers. In previous studies, Wang *et al.* designed a Voronoi porous scaffold with graded distribution in the *z*-axis direction, which lacked clear graded distribution standard[12]. Deering *et al.* generated an anisotropic Voronoi porous implant by dividing the plane unevenly along the *z*-axis direction, which was too subjective to reflect the graded distribution of natural bone[19]. In addition, Liu *et al.* established an elasticity-to-density mapping model, and generated FGPMs based on the Voronoi tessellation, which relied on the intensive division of a finite element mesh, resulting in a huge amount of data[20]. From the above studies, it is clear that there are still many limitations in the current research and the designs of FGPMs. In addition, there are few studies on controllable and graded design of the bionic bone scaffolds, and many pivotal problems still remain unsolved.

Topology optimization is the most classic method of mechanical optimization. According to the mechanical conditions and the optimization objectives, researchers can obtain the optimal configuration of the internal structure of the model through iterative calculation of finite element analysis, and they can achieve the optimal distribution of materials with respect to the targeted performance[21,22]. Many studies believe that FGPMs and topology optimization methods are highly unified in nature[23,24], and that the latter can be used as the basis for FGPMs design[25,26]. For example, Alzahrani *et al.* proposed a relative density mapping (RDM) method, which introduced the topology optimization method into the lattice structure design[27]. In addition, Zhao *et al.* used the local relative density mapping method to generate the corresponding two-dimensional cellular porous structure according to the optimized solid isotropic material with penalization (SIMP) continuum topology optimization results with variable density[28]. Wang *et al.* carried out concurrent design of hierarchical structures for regular porous structures according to the results of continuum topology optimization[29]. Radman *et al.* optimized the topology of the porous structure with regular basic structure units, which showed the characteristic of graded distribution of density[26]. It was found that the FGPMs design, using topology optimization information, targets mainly the two-dimensional regular porous structures or the three-dimensional (3D) structures with repeated simple basic structural units. Introducing the topology optimization into the bionic bone scaffolds design field has broad prospects. In engineering applications, the bi-directional evolutionary structural optimization (BESO) is widely used as a common topology optimization method. The simultaneous deletion and growth of materials reflects the bidirectional nature of the BESO method, which greatly ensures the geometric and mechanical continuity of the topology optimization continuum. BESO reduces the maximum stress inside the structure to the greatest extent, providing a highly accurate solution for optimizing the stress distribution inside the structure[30-32]. In addition, the results of BESO can show the main load-bearing area and the force transfer path inside the macroscopic model[33,34]. It is a pioneering and a reasonable attempt to take the BESO information as the design basis of the bionic bone scaffolds, and to show how to establish the relationship between the topology optimization design and the porous structure design. This will present the main challenge in this work.

In our previous studies, a parametric design method of the porous scaffolds based on the Voronoi tessellation was proposed, and the mechanical and biological properties were fully discussed[12,13,35,36]. Regrettably, however, our
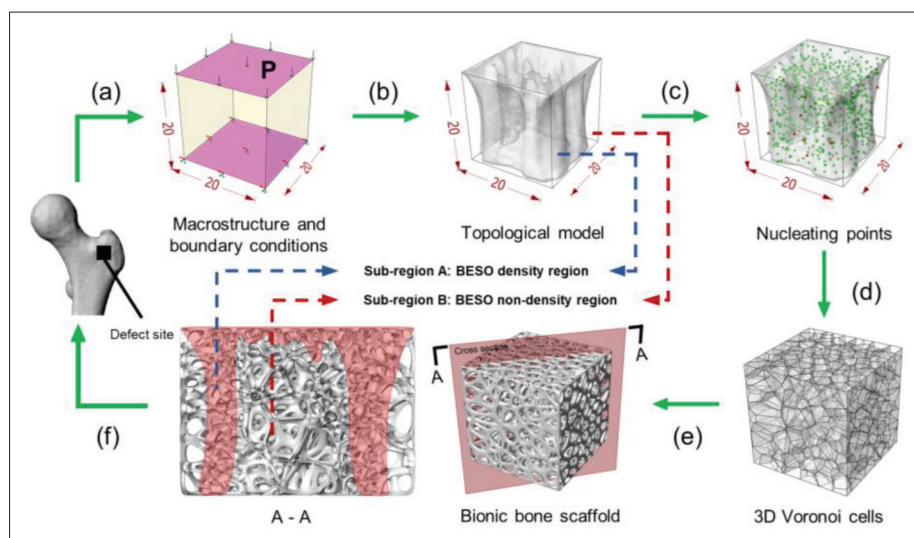
Figure 1. Design procedures for the bionic bone scaffold.

previous design method did not implement the graded distribution of the characteristic parameters, which is the most critical design of the bionic bone scaffolds. Referring to previous studies, we propose in this work a sub-regional design methodology of the bionic bone scaffolds, based on the macrostructural topology and the **Voronoi tessellation**. It is worth pointing out that the definition of macrostructure in this paper is the original model for BESO while the corresponding microstructure represents the FGPMs populated in the design domain. The design domain is divided into sub-region A (representing the BESO density region) and sub-region B (representing the BESO non-density region) as the guideline for pores' graded design. It is worth noting that, with a mechanical continuity concern, the porosity and the aperture values in sub-region B follows the distance-to-scale coefficient mapping model, presenting a gradient change. Additionally, the as-designed models were analyzed in this work through mechanical simulation and were validated after being fabricated by the LPBF process, using the Ti-6Al-4V powder, to study the quasi-static compressive behavior. Notably, this approach considers the overall problem of shape and the property control under the synergistic constraints of mechanics, biology, geometry, and LPBF process, and it delivers a full discussion regarding the influence of irregularity and scale coefficient on mechanical properties of the as-built specimens.

This paper is divided as follows: section 2 presents the design and the methodology approaches; section 3 shows the obtained results, from a simulation and implementation points of view, and the comparison; and the last section concludes this work and proposes some ideas, which will be implemented in future.

2. Design and methods

The BESO methodology was introduced to realize the macrostructural topology in this paper. The bionic bone scaffolds were designed using the novel CAD software Rhinoceros3D© (Robert McNeel & Associates, v.7.0 SR4) with the plugin Grasshopper™ v.1.0.0007. The flow chart in Figure 1 illustrates the procedures for modeling this bionic bone scaffold, including (a) bone defect site analysis, (b) macrostructural topology, (c) Boolean operation according to the combined probability sphere model, (d) 3D Voronoi tessellation based on the graded nucleating points, (e) porosification based on the distance-to-scale coefficient mapping model, and finally (f) fabrication and implantation.

2.1. Design and parametric characterization of the bionic bone scaffolds

To realize the most reasonable graded distribution, the topological information of the macroscopic model is needed. Based on the axiom of the uniform strain energy density, the maximization structural strength requires minimizing the strain energy[37]. In this paper, the design variable is the unit density, and the optimization objective is to minimize the strain energy of the macrostructure. The mathematical model of strength optimization under the constraint of equilibrium equation is expressed as follows:

$$U(\rho_i) = \frac{1}{2}P^T\delta$$
$$s.t.\ K^T\delta = P$$
$$\sum_{i=1}^{n}V_i\rho_i - f_v V^* = 0 \qquad (I)$$
$$E_i = \rho_i^p E_i^*$$
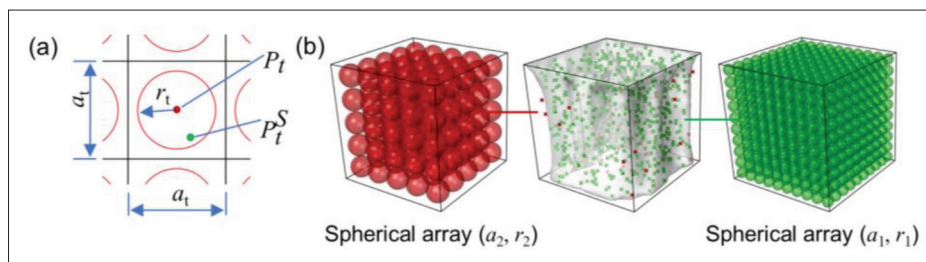$$\rho_i = \rho_{min}\ or\ 1$$

Figure 2. Generation of the graded Voronoi nucleating points where one can see (a) design parameters of the combined probability sphere model, (b) combined probability sphere model and Voronoi nucleating points, where $\{P_{1i}^S\}_{i=1}^N$ is marked red while $\{P_{2j}^S\}_{j=1}^M$ is marked green.

where $i = 1, 2, …, n$ represents the volume mesh number of the macroscopic model and ρ_i is a binary design variable representing the cell density of the i-th volume mesh. A mesh cell is considered deleted when $\rho_i = \rho_{min}$, and it is considered reserved when $\rho_i = 1$. The variables U, K, δ, and P represent, respectively, the strain energy, the total stiffness matrix, the displacement vector, and the external load vector acting on the structure. V_i is the volume of the i-th volume mesh cell while V^* is the initial volume of the macroscopic model. f_v is the volume fraction coefficient, representing the ratio of the target volume to the initial volume. In addition, E_i^* and E_i represent, respectively, the elastic modulus of the i-th volume mesh cell before and after the topological optimization. Finally, the penalty coefficient p has a fixed value (equal to 3) in this work referring to previous studies[38].

It is obvious that the 20 × 20 × 20 mm³ design domain was divided into two sub-regions by the topological model. After extensive tests, it was found that arranging nucleating points only in sub-region A leads to extremely poor geometric continuity. Meanwhile, open meshes were even observed, leading to forming failure. Therefore, this study improved the methodology of generating controllable nucleating points that was adopted in previous studies[12], proposing a combined probability sphere model where a_1 and a_2 are the dot pitch of sphere centers ($a_1 > a_2$). It is worth noting that the following constraints were added:

(i) $r_1 / a_1 = r_2 / a_2$ for the purpose of ensuring geometric continuity and design controllability, where r_1 and r_2 represent the radius of spheres generated from regular dot matrices P_{1i} and P_{2j}, respectively;

(ii) $0 < r_t < a_t / 2$ where $t \in \{1,2\}$ is a binary design variable, representing two different types of the regular dot matrix.

The same r / a value provided an extremely high controllability and consistency to the design procedure, effectively alleviating the possible stress concentration and geometric mutation phenomenon. The Boolean operation process based on the combined probability sphere model is shown in Figure 2. It is worth pointing out that the values
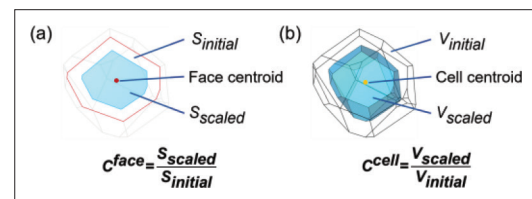

Figure 3. Definition of the scale coefficient where one can see (a) C^{face} and (b) C^{cell}.

of a_t and r_t are indeterminate, and the specific values will be discussed in section 3. For random points P_1^S, generated from the probability sphere model with dot pitch of a_1, the Boolean operation was used to get a point set $\{P_{1i}^S\}_{i=1}^N$ in sub-region B. In contrast, only the interior and the surface points in sub-region A were retained as a point set $\{P_{2j}^S\}_{j=1}^M$ for P_2^S. By combining these two sets of points $\{P_{1i}^S\}_{i=1}^N$ and $\{P_{2j}^S\}_{j=1}^M$, a set of irregular points $\{S_k\}_{k=1}^{N+M}$ was defined as the nucleating points of the bionic bone scaffolds. The irregularity ε of this scaffold is defined by the distance from a random point P_t^S to its corresponding probability sphere center P_t:

$$\varepsilon = \frac{1}{N+M}\left(\sum_{i=1}^N \frac{dist(P_{1i}, P_{1i}^S)}{a_1} + \sum_{j=1}^M \frac{dist(P_{2j}, P_{2j}^S)}{a_2} \right) \quad (II)$$

where N and M represent, respectively, the quantities of P_1^S and P_2^S after the Boolean operations. The number of nucleating points (NNP) is equal to the sum value of N and M ($NNP = N + M$). The variables $dist(P_{1i}, P_{1i}^S)$ and $dist(P_{2j}, P_{2j}^S)$ denote the distance from the random point P_t^S to the center of its corresponding probability sphere P_t in 3D Euclidean space. Since the radius of the probability sphere was restricted, ε can be easily deduced ($0 < \varepsilon < 0.5$).

The point set $\{S_k\}_{k=1}^{N+M}$ was processed using the Voronoi 3D Grasshopper™ plugin to obtain the 3D Voronoi cell structure. The scale coefficient C was introduced to realize the deflation of Voronoi faces and the Voronoi cells. As shown in Figure 3, C can be further divided into two variables, C^{face} and C^{cell}, where they represent, respectively,
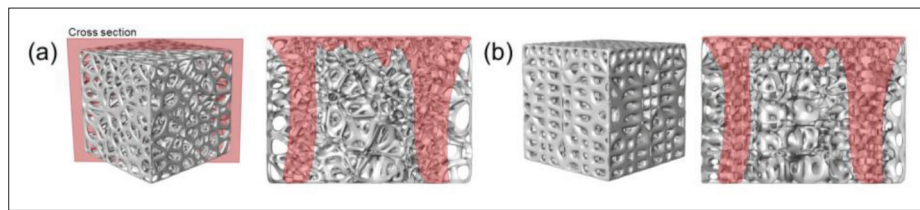
Figure 4. The as-designed models where a_1 = 4000 μm and a_2 = 2000 μm are held constant and the set of values of C_1, C_2, and ε are respectively (a) 50%, 90%, and 0.47 and (b) 20%, 80%, and 0.06.

the scaling of Voronoi face (Figure 3a) and of Voronoi cell (Figure 3b) with respect to their corresponding centers.

In addition, the bionic bone scaffolds should have specific regional functionality; this will require that the graded distribution of pore locations should be considered, and more importantly, the graded porosity should also be taken into account. A distance-to-scale coefficient mapping model, based on the shortest distance from $\{P_{1i}^{S}\}_{i=1}^{N}$ to sub-region A, was computed, where its core is calculating the shortest distance d_i (i = 1, 2, …, N) from each point in the point set $\{P_{1i}^{S}\}_{i=1}^{N}$ to the topological model that is determined. The values were ordered from smallest to largest and the maximum value d_{max} in d_i was determined. Thus, C^{cell}, corresponding to the *i-th* nucleating point, can be described as follows:

$$C_i^{cell} = C_1 + \frac{d_i}{d_{max}}(C_2 - C_1) \qquad (III)$$

where C_1 represents the lower limit of the predefined value of the scale coefficient while C_2 corresponds to its upper limit. The value $C^{cell} = C_1$ was set for the Voronoi cells in sub-region A while in sub-region B, the value of C^{cell} was set to a graded value ranging between C_1 and C_2, depending on the mapping model. The gradient setting of C^{cell} in sub-region B was aimed to maximize the mechanical continuity and enhance the regional functionality of cell adhesion, especially alleviating the mutation phenomenon at the junction of the two sub-regions.

Almost all studies did not distinguish between C^{cell} and C^{face}, which exhibited a lack of adaptability to this bionic bone scaffold. Previous work has shown that the dot pitch is the most important factor influencing the aperture at a certain scale coefficient[12,13]. Due to the introduction of the combined probability sphere model, the nucleating points were mainly concentrated in sub-region A, which already resulted in a graded distribution of aperture. When the same scale coefficient used for C^{cell} is applied to C^{face}, it will lead to a large increase in aperture less than 60 μm and greater than 1200 μm, significantly reducing the functionality of the scaffolds to induce osteoblasts in order to proliferate and differentiate in sub-region B. To

solve the problem, this study proposed a solution through the following relational formula:

$$C_i^{face} = C_1 + C_2 - C_i^{cell} = C_2 - \frac{d_i}{d_{max}}(C_2 - C_1) \qquad (IV)$$

Then, the final 3D porous interconnection structure was obtained by the Boolean operation between the initial 3D Voronoi cell structure and the scaling results. Finally, Weaverbird v.0.9.0.1 was used to soften the trabecular-like mesh model. Figure 4 shows the as-designed models with different design variables. It is clear that each characteristic parameter has achieved the predetermined design goal.

It is important to mention that the porosity of the bionic bone scaffolds can be parametrically modified by changing C_1 and C_2. Similarly, the specific surface area can be adjusted, when needed, at constant porosity by controlling the dot pitch and the scale coefficient. Equation IV brings an extremely great improvement to the specific surface area in sub-region B, which positively induces the adhesion and proliferation of osteoblasts. The effect of specific surface area on permeability will be investigated in a future work. The aperture D (defined by the equivalent diameter method) of the bionic bone scaffolds is affected by the synergy of C^{face} and the design variables of the combined probability sphere model. The target aperture range can be obtained by adjusting C^{face} when the probability sphere model is determined. Furthermore, it is worth pointing out that our approach is applicable to any type of 3D printers.

2.2 Finite element analysis of the bionic bone scaffolds

As mentioned in section 2.1, the graded Voronoi nucleating points have a random distribution, and the randomness arises from the combined probability sphere model. In order to evaluate the effect of randomness on the mechanical properties and the porosity, four as-designed models, denoted as randomness series, were generated using four different random seeds. Other design parameters were kept the same where a_1 = 4000 μm, a_2 = 2000 μm, C_1 = 50%, C_2 = 90%, and ε = 0.47. Moreover, the dot pitch a_t was supposed to be another possible factor that affect the mechanical properties of the bionic bone scaffolds. Two series of the as-designed models with different a_1

Table 1. LPBF process parameters

	Laser power (W)	Scanning speed (mm/s)	Hatch spacing (mm)	Layer thickness (mm)	Laser focus (mm)	Atmosphere
Value	160	1250	0.08	0.03	0.08	Ar

values (denoted as a_1 series) and a_2 values (denoted as a_2 series) were set up to evaluate the effect of dot pitch on the mechanical properties and the porosity, where a_2 = 2000 μm (for a_1 series) and a_1 = 4000 μm (for a_2 series) were held constant. Other design variables were kept the same as those in randomness series.

To assess the expected mechanical behavior of the as-designed models, the finite element analysis (FEA) on ideal as-designed models was performed using the commercial software Workbench (ANSYS, Inc., v.18.0). The FEA models were assumed to be linear, elastic, and homogeneous. The material properties were set to Ti-6Al-4V, where Young's modulus was equal to 113.8 GPa, Poisson's ratio equal to 0.342, and the yield stress equal to 895 MPa. The loading conditions and the boundary constraints were as follows: the top of the as-designed model was loaded with a pressure of 80 MPa while the bottom boundary was fixed. The stress distribution under pressure was investigated through parameter settings and model meshing and solving. The mechanical properties of the as-designed models were evaluated by the maximum Von-Mises stress value under the same loading condition.

2.3 Fabrication and compressive testing of the bionic bone scaffolds

The as-built specimens were fabricated using the LPBF machine (NCLM2120, China). The process parameters, optimized by orthogonal tests, are shown in Table 1. The commercial Ti-6Al-4V extra low interstitial (ELI) powder supplied by EOS GmbH was used in the experiment, meeting ISO 5832-3 and ASTM F1472 norms.

The characteristic parameters that affect the mechanical properties of the porous biomaterials mainly include porosity and aperture. Generally, the effect of porosity is dominant[39,40]. Irregularity is also one of the possible influences due to the introduction of the probability sphere model. In this study, two sets of uniaxial compression tests were set up to investigate the effects of irregularity and of graded porosity on the compressive performance. As shown in Table 2, the as-built specimens with different ε values were denoted as irregularity series and those with different combinations of C_1 and C_2 values were denoted as scale coefficient series. The other design variables were as follows: a_1 = 3333 μm and a_2 = 1333 μm. Besides, a solid part of $20 \times 20 \times 0.5$ mm³ was fixed at the top and at the bottom acting as the compensation area for the wire-electrode cutting process and the boundary area for the

Table 2. Design parameters of as-built specimens

Series	No.	C_1 (%)	C_2 (%)	ε
Irregularity series	01	50	90	0.06
	02			0.12
	03			0.18
	04			0.25
	05			0.30
	06			0.39
	07			0.47
	08			0.50
Scale coefficient series	09	50	90	0.47
	10	50	80	
	11	50	70	
	12	50	60	
	13	60	90	
	14	70	90	
	15	80	90	

compression test. Note that three identical specimens were prepared for each model and the test results represent the average values of these specimens.

According to the national standard GB/T 31930-2015, the static compression tests were performed using a universal testing machine (UTM5305H) at a constant speed equal to 0.5 mm/min. The loading and displacement were recorded until the struts broke. Known as apparent elastic modulus of cellular metals, the elastic modulus represents the slope of the elastic straight lines, determined by the elastic loading between 70% and 20% of plateau stress. The ultimate strength was defined by the first maximum compressive strength, which determined the load-bearing capacity of the as-built specimens.

3. Results and discussion

3.1. Relationship between design variables and characteristic parameters

Different combinations of dot pitch should be discussed first, as this paper presented a combined probability sphere model. It is obvious from section 2.1 that adjusting the dot pitch essentially controls the upper limit of the aperture. The first step was to determine the range of a_1 in order to meet the optimal aperture (60–1200 μm) for bone implants[11,41]. The values of a_1 for the as-designed models

Table 3. Values of a1 for different scale coefficients

C (%)	a_1 (μm)	r_1 (μm)	Davg (μm)
50	3333	833	1127
60	2857	714	1131
70	2500	625	1139
80	2222	555	1139
90	2000	500	1138

with different scale coefficients are shown in Table 3, where D_{avg} refers to the average aperture. Figure 5a–c depict the aperture frequency distribution when the value of a_1 changes. Note that the aperture frequency refers to the ratio of the number of occurrences of a certain aperture value to the total number of pores. It is clear that a_2 is the dominant factor influencing the aperture distribution. In addition, the influence of a_1 on the aperture distribution becomes smaller as a_2 decreases, which is shown by the increasing similarity of the aperture frequency curves. Therefore, a large a_1, within a reasonable range, can be set to improve the computational efficiency. However, it will lead to a significant increase in the proportion of apertures smaller than 60 μm when a_2 takes a too small value, affecting the permeability of the scaffolds. Therefore, based on extensive simulations, the values of a_1 and a_2 equal to 3333 μm and 1333 μm, respectively, in this study were chosen. These values are suitable for this macrostructure,

taking the target aperture range and computational efficiency into account. Besides, randomness was supposed to be one of the possible influencing factors of the aperture distribution as the generation of Voronoi nucleating points relied on the random seeds. Therefore, five samples were generated with different random seeds and the aperture distribution is shown in Figure 5d. It is obvious that although there were perturbations in aperture frequency curves, the overall distribution remained the same and the perturbations occurred mainly ranging from 100 μm to 1000 μm, with little effect on the actual bone implantation performance. To conclude, the combined probability sphere model design was effective, and the tests were highly reproducible.

Figure 6a shows that there is a strong linear relationship between ε and r / a. Irregularity of the bionic bone scaffolds is linked to the ratio of r / a in this study to simplify the calculation process. Variations of characteristic parameters with different values of ε are shown in Table 4, where Φ refers to the porosity. It is clear that D_{avg} and Φ are proportional to ε when $\varepsilon < 0.3$, and tend to stabilize when $0.3 \leq \varepsilon < 0.5$. NNP decreases gradually as ε increases, which is attributed to the increase in probability of random points appearing in sub-region B as the range of perturbations increases. In general, the influence of ε on NNP can be ignored when $\varepsilon < 0.5$. Notably, it is found that Φ and NNP decrease significantly when $\varepsilon = 0.58$, further validating the rationality of its value range. As for Figure 6b, it
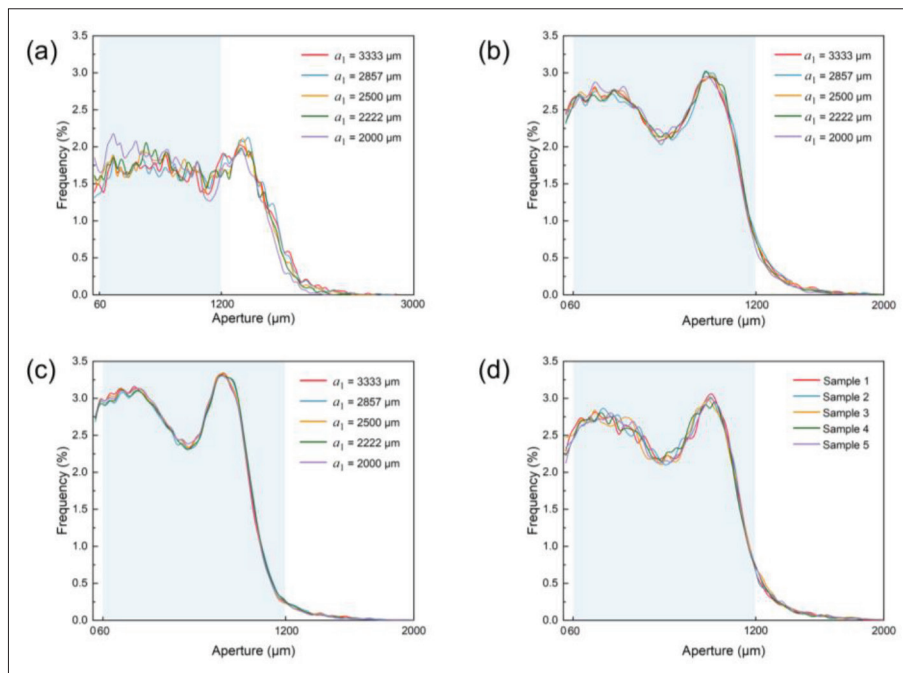

Figure 5. Aperture frequency distribution of the as-designed models with design parameters of C_1 = 50%, C_2 = 90%, and ε = 0.25 where (a) a_2 = 2000 μm, (b) a_2 = 1333 μm, (c) a_2 = 1000 μm, and (d) influence of randomness.
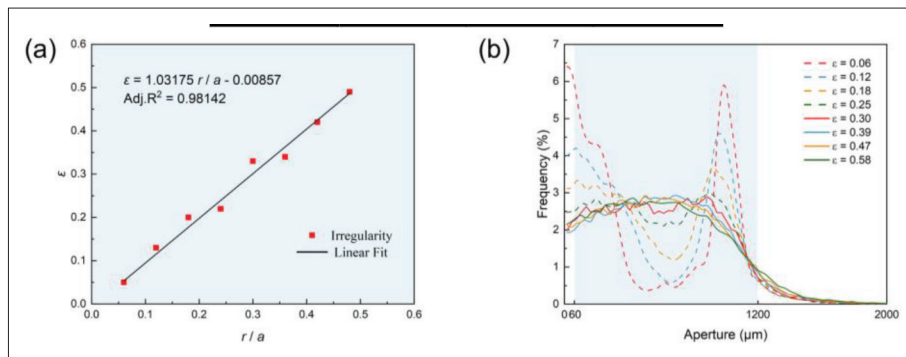
Figure 6. The as-designed models with different values of ε where (a) represents the relationship between r/a and ε, and (b) shows the influence of ε on the aperture frequency distribution.

Table 4. Relationship between ε and the characteristic parameters

E	NNP	Φ (%)	Davg (μm)
0.06	2498	67.90	641.70
0.12	2487	69.88	673.78
0.18	2484	69.24	696.02
0.25	2482	70.26	716.32
0.30	2480	72.28	729.88
0.39	2483	72.63	730.57
0.47	2479	72.43	730.18
0.58	2435	69.05	730.16

shows the aperture frequency curves for different values of ε. Specifically, the quantity of the apertures at 15 μm and 1000 μm levels is significantly larger when ε ≤ 0.25, leading to excessive span of the apertures and causing discontinuities in the mechanical properties. At the same time, the proportion of apertures smaller than 60 μm is too high and the positive stimulus to induce osteoblast adhesion and proliferation is lost, affecting the actual performance of the bone implants. The aperture values are mainly in the range between 60 μm and 1200 μm when ε > 0.25, and there will be no sudden changes in mechanical properties at vulnerable parts when the aperture values fall within the range.

Figure 7a and b present the influence of the scale coefficient on the porous biomaterials in sub-region A. Figure 7a, where C^{cell} is maintained constant, demonstrates the effect of a single factor C^{face}. It is obvious that different values of dot pitch have little effect on Φ, which is consistent with our previous works[12,13]. Apart from that, D_{avg} and Φ are proportional and linearly related to C^{face}. Figure 7b, where C^{face} is maintained constant, demonstrates the effect of C^{cell}. Similarly, the different dot pitch values have little effect on Φ, which is proportional and linearly related to C^{cell}. However, D_{avg} remains unchanged as C^{cell} increases

when the value of dot pitch is determined, which indicated that the aperture is only controlled by C^{face}.

Figure 7c shows the gradient change of the characteristic parameters. It can be observed that D_{avg} decreases when the ratio C^{cell}/C^{face} increases, which is diametrically opposed to the results of previous studies setting $C^{cell} = C^{face}$ as shown in Figure 7d. This peculiar phenomenon illustrates the effectiveness of the design, ensuring the mechanical continuity of sub-region B and increasing the specific surface area, leading to an improvement in the bio-functionality. An upward trend of Φ is shown, indicating that the graded porosity distribution is realized. With the simplification according to Equation IV, the relationship between C^{cell}/C^{face} and Φ can be fitted and a unary expression is shown as follows:

$$\Phi = (91.94915 - 20.31354e^{-\frac{(\frac{C^{cell}}{140-C^{cell}}-0.60613)^2}{1.61989}}) \times 100\% \quad (V)$$

The local porosity can be calculated as shown in Figure 7e. Figure 7f shows the change of the overall porosity. It is clear that the scale coefficient exhibits a strong linear relationship with the porosity. The overall target porosity of the bionic bone scaffolds can be controlled by the scale coefficient.

The above results demonstrate that the as-designed bionic bone scaffolds are highly controllable. Design variables can be flexibly adjusted to accommodate the changes of the target characteristic parameters. In addition, the results of the aperture frequency diagrams demonstrate the superiority and the effectiveness of this methodology to achieve an optimal aperture distribution for porous biomaterials. Since the aperture is a complex function of the C^{face}, a_t, r_t, and d_t, this task will be developed in a future study. The discussion on the scale coefficient proves that the as-designed models achieve a graded distribution of porosity, which could be accurately calculated based on Equation V.
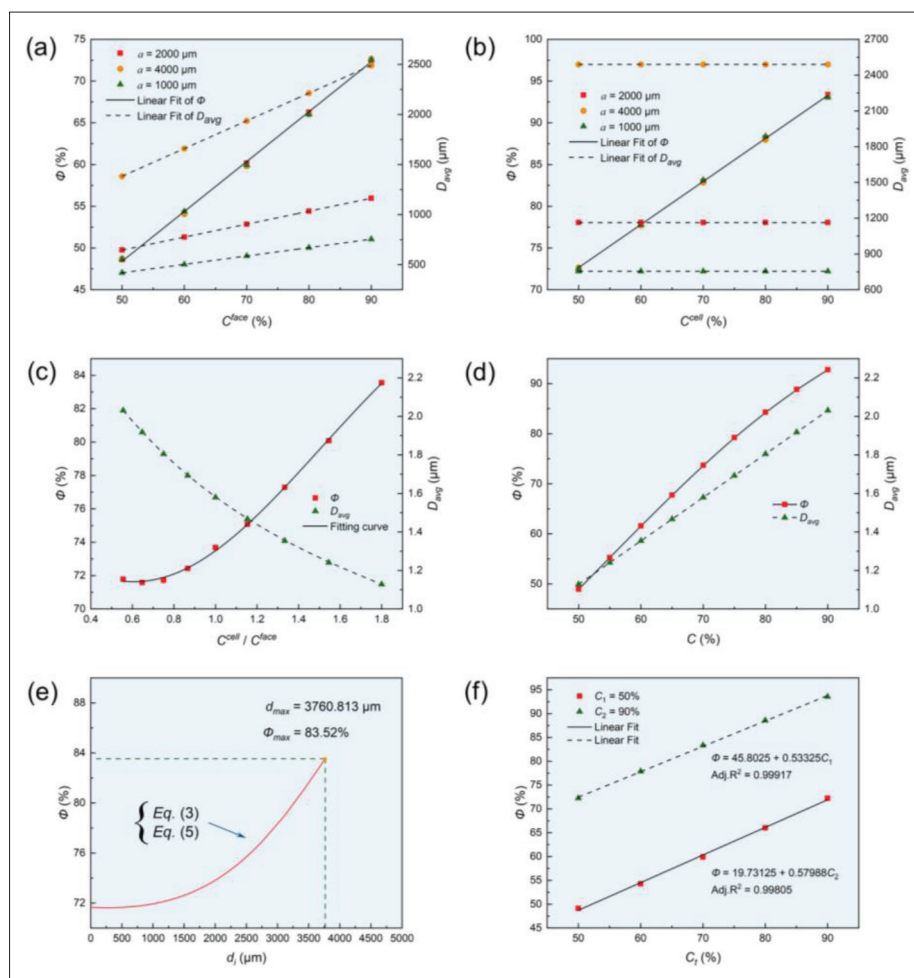
Figure 7. Characteristic parameters of the as-designed models with ε = 0.47 where one can see (a) influence of C^{face} where C^{cell} = 50%, (b) influence of C^{cell} where C^{face} = 90%, (c) variation trend with C^{cell} / C^{face}, (d) variation trend with C ($C^{cell} = C^{face}$), (e) influence of d_i, and (f) influence of C_i.

3.2. Finite element analysis of as-designed models

Randomness arose from the combined probability sphere model in this study. Figure 8 shows the FEA result of the four as-designed models in randomness series. The four models share roughly the same stress nephogram. The range of maximum von Mises stress values varies between 1403.27 MPa and 1468.75 MPa. Meanwhile, the range of porosity values varies between 72.33% and 73.08%. The results demonstrate that randomness has a negligible effect on stress distribution and porosity, further verifying the feasibility of the combined probability sphere model.

Similarly, it can be concluded from Figure 9a that a_1 has little effect on the compressive property of the as-designed models. The maximum von Mises stress and porosity reach value ranges of 1423.95–1497.63 MPa and 72.83%–74.55%, respectively. With the increase of a_1, stress nephograms are basically unchanged, which means that *NNP* in sub-region B has a negligible effect on the mechanical property and the porosity. As depicted in Figure 9b, the

FEA models in a_2 series have maximum von Mises stress values of 1427.63 MPa, 1718.27 MPa, 2106.50 MPa, and 2842.75 MPa, respectively. In addition, the corresponding values of porosity are 72.62%, 72.13%, 71.61%, and 73.92%, respectively. More struts exceed the yield strength as the value of a_2 increases, which means *NNP* in sub-region A has a greater influence on the mechanical property.

Randomness and a_1 bring a small change to *NNP* while a_2 is the opposite, as it has a great influence on the structural strength, which shows a great consistency with the discussions in section 3.1. The reason for variation of *NNP* in randomness series was the random perturbation of points, which resulted in a perturbation in the number of points retained and deleted by the Boolean operation.

3.3. Mechanical characterization of the as-built specimens

The as-built specimens fabricated by LPBF are shown in Figure 10. For ease of labeling in the figure, the as-built
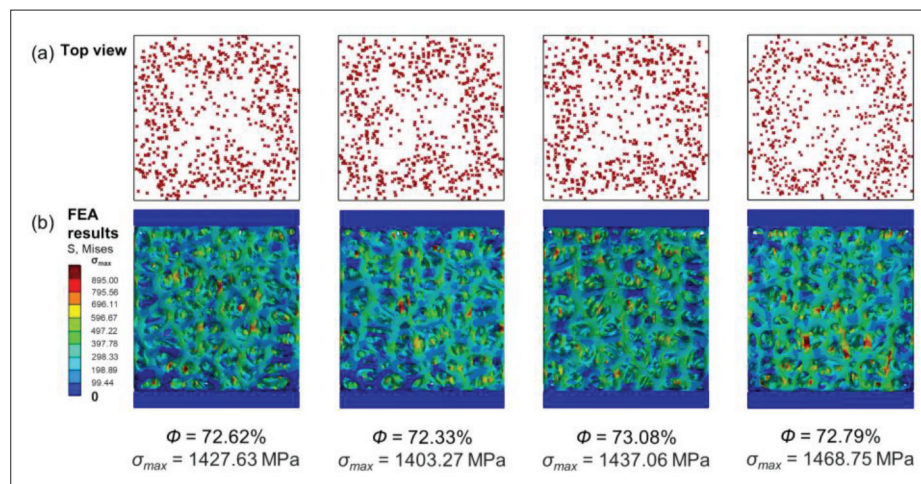
Figure 8. FEA results of randomness series where one can see (a) the top view of the Voronoi nucleating points and (b) the stress nephograms.
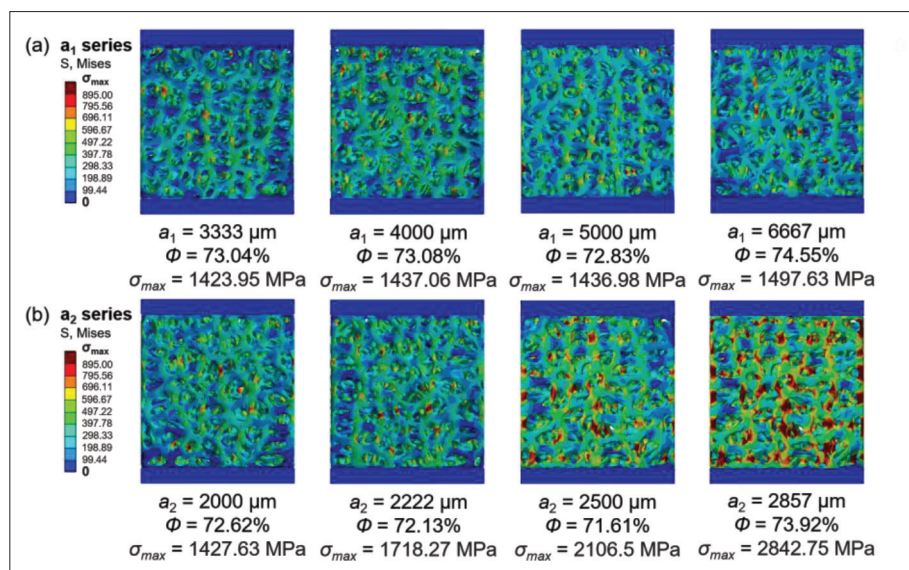

Figure 9. FEA results where one can see the stress nephograms of (a) a_1 series and (b) a_2 series.

specimens were numbered (refer to Table 2). Table 5 lists the porosity of the as-designed models and the as-built specimens. The deviation of porosity between models and specimens is less than 4%, demonstrating that all struts were precisely manufactured to a predetermined size and shape.

The results of the static compression tests of the as-built specimens are summarized in Figure 11. The stress–strain curves are typical for the as-built specimens, including the linear increase in stress and a plateau region with fluctuating stresses. Meanwhile, an initial approximate parabola is observed in each stress–strain curve, going upwards at the beginning of loading. This might be attributed to the lack of fusion powder from manufacturing defects, which may

lead to an uneven contact interface between pressure head and specimens[36,42,43].

Apparent elastic modulus (E) and ultimate strength (S) are the pivotal characteristic parameters for evaluating the mechanical properties of porous biomaterials. As depicted in Figure 12a and d, specimens with constant design parameters of $C_1 = 50\%$ and $\varepsilon = 0.47$ (No. 09, 10, 11, and 12) have an ultimate strength range of 190.19–268.03 MPa. Meanwhile, the corresponding elastic modulus reaches a value range of 4.52–7.12 GPa. Given a certain C_1 and ε, the as-built specimens with a larger C_2 have a higher porosity value (refer to Table 5), which results in a smaller apparent elastic modulus and an ultimate strength. This result is consistent with the classic foam metal model[44,45]. With the
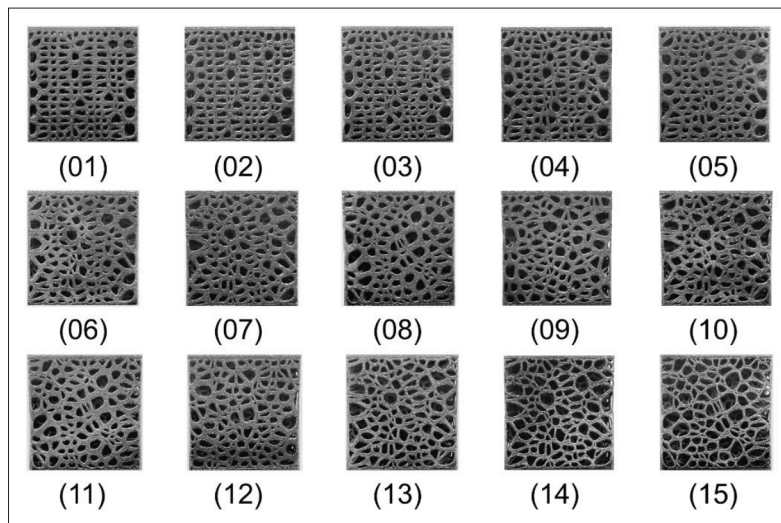
Figure 10. Bionic bone scaffolds fabricated by LPBF process.

Table 5. Porosity of the as-designed models and the as-built specimens

Part number	Porosity (%)		Deviation (%)
	3D model	LPBF specimen	
(01)	67.90	65.33	2.57
(02)	69.88	68.75	1.13
(03)	69.24	66.93	2.31
(04)	70.26	68.45	1.81
(05)	72.28	69.66	2.62
(06)	72.63	70.59	2.04
(07)	72.43	71.36	1.07
(08)	71.05	69.84	1.21
(09)	72.25	70.06	2.19
(10)	66.03	64.97	1.06
(11)	59.93	57.27	2.66
(12)	54.29	53.18	1.11
(13)	77.89	75.94	1.95
(14)	83.36	79.83	3.53
(15)	88.59	85.08	3.51

application of Gibson–Ashby model[46,47], the expressions can be fitted as follows:

$$S = 375.64(1 - \frac{\Phi}{100})^{0.52} \tag{VI}$$

$$E = 16.27(1 - \frac{\Phi}{100})^{1.06} \tag{VII}$$

Similarly, the ultimate strength of specimens with constant design parameters of $C_2 = 90\%$ and $\varepsilon = 0.47$ (No. 09, 13, 14, and 15) ranges from 38.55 to 190.19 MPa

(refer to Figure 12b). Meanwhile, Figure 12e depicts that the corresponding elastic modulus reaches a value range of 1.5–4.52 GPa. Thus, the Gibson–Ashby formula can be rewritten as follows:

$$S = 1551.18(1 - \frac{\Phi}{100})^{1.63} \tag{VIII}$$

$$E = 20.83(1 - \frac{\Phi}{100})^{1.17} \tag{IX}$$

The increasement of C_1 and C_2 leads to a greater porosity. The diameter of struts decreases accordingly, resulting in the decay of stiffness and an easier deformation. Figure 13 shows the growth rate diagrams of E and S as porosity decreases. In this study, the growth rate is defined as the ratio of ΔS (ΔE) to S_0 (E_0), where the corresponding value of S (E) is determined as S_0 (E_0) when design variable C_1 or C_2 takes the value of its upper limit. When the porosity is determined only through the variable C_2 ranging from 60% to 90% with a constant $C_1 = 50\%$ (No. 09, 10, 11, and 12), the ultimate strength increases by 10% as C_2 decreases by about 10% (Figure 13a). The growth rate of E is slightly higher than that of S. Similarly, when the porosity is determined only through the variable C_1 ranging from 50% to 80% with a constant $C_2 = 90\%$ (No. 09, 13, 14, and 15), S and E increase significantly with the decrease of C_1. As depicted in Figure 13b, the growth rate of S is almost 10 times greater than that in Figure 13a as C_1 decreases by 10%. Given a certain $C_1 = 50\%$, porous biomaterials in sub-region A have a constant C^{cell} value equal to 50% and a variable C^{face} value ranging between 60% and 90%. S increases as C^{face} decreases, but the amplitude of the change is not significant. Similarly, given a certain $C_2 = 90\%$, porous biomaterials in sub-region A have a constant C^{face} value equal to 90% and a variable C^{cell} value ranging between 60%
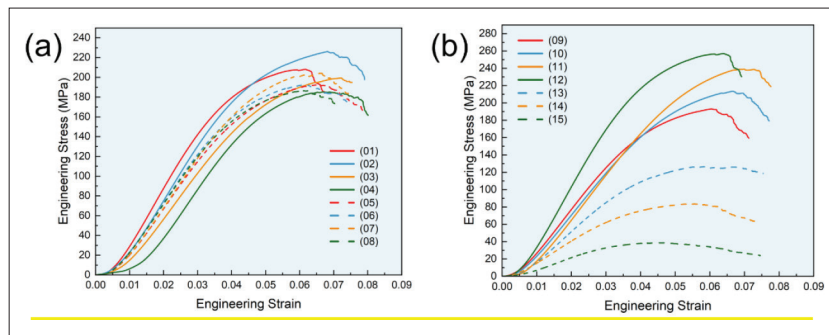
Figure 11. Static compression tests for (a) irregularity series and (b) scale coefficient series.
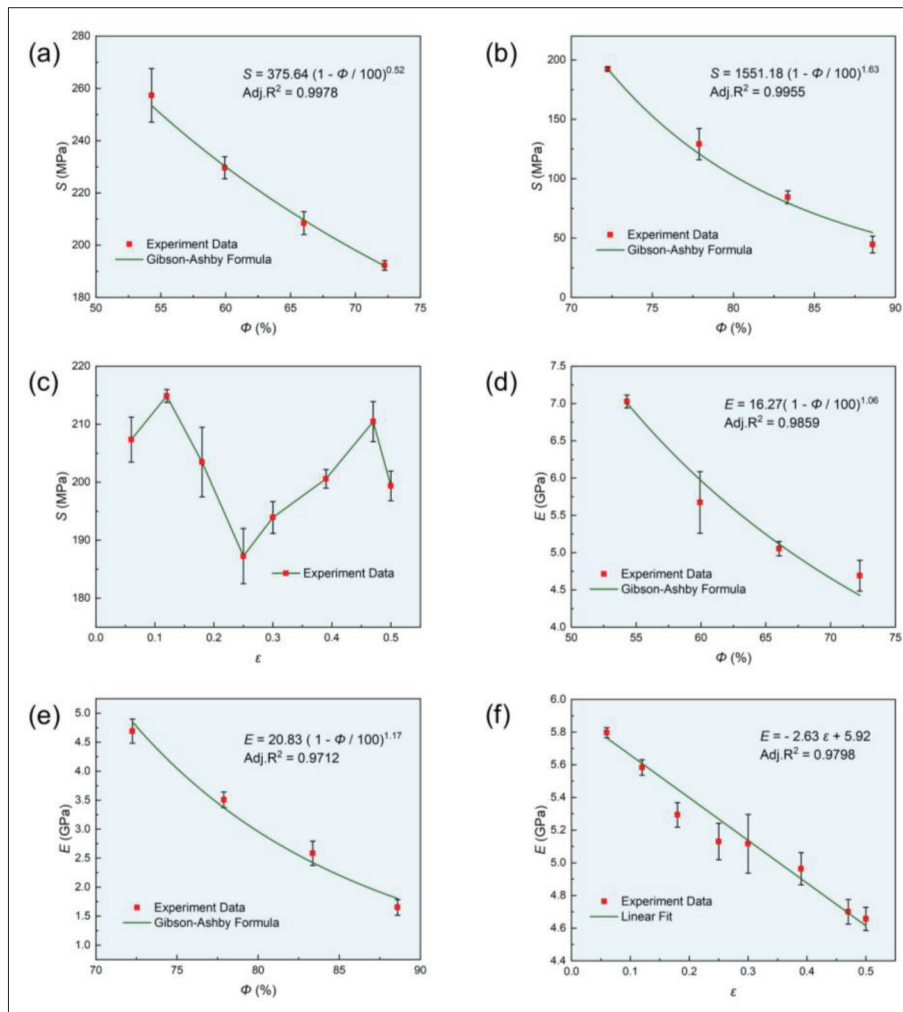

Figure 12. Mechanical properties calculated from raw data for (a) S of specimens with variable C_2, (b) S of specimens with variable C_1, (c) S of specimens with variable ε, (d) E of specimens with variable C_2, (e) E of specimens with variable C_1, and (f) E of specimens with variable ε.

and 90%. S increases as C^{cell} decreases, and the magnitude of the change is much larger than the former case. It can be concluded, by comparison, that the compressive properties of the as-built specimens are closely related with C^{cell} and C^{face}, where C^{cell} is considered dominant. The effectiveness of this design method is proven according to the growth rate results. The strength of porous biomaterials is mainly controlled by the porosity in sub-region A. Meanwhile, the results are consistent with findings in section 3.1 and section 3.2.
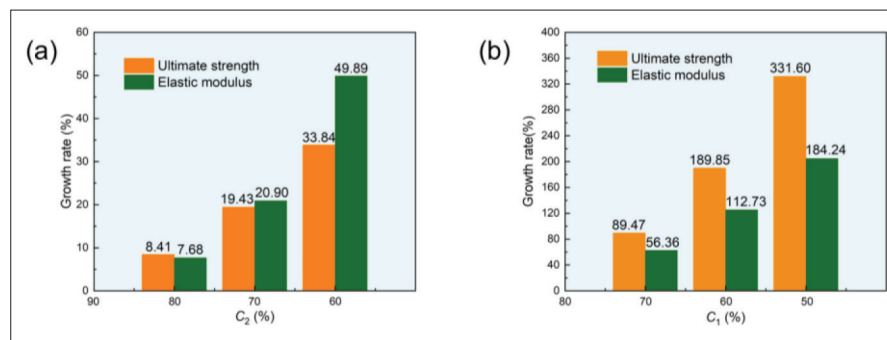
Figure 13. Growth rate of S and E for (a) C_1 = 50% and (b) C_2 = 90%.

As shown in Figure 12c and f, specimens in irregularity series have an apparent elastic modulus range between 4.67 GPa and 5.83 GPa. E decreases almost linearly as irregularity increases. Meanwhile, S reaches a value range of 182.51–216.14 MPa, showing an irregular change trend, different from E. For instance:

(i)　S of the as-built specimen, with $\varepsilon = 0.12$, is equal to 216.14 MPa, which is the maximum value in ε series whereas the corresponding value of E is 5.62 GPa;

(ii)　S of the as-built specimen, with $\varepsilon = 0.25$, is equal to 182.51 MPa, which is the minimum value whereas the corresponding value of E is 5.23 GPa;

(iii)　S of the as-built specimen, with $\varepsilon = 0.47$, is equal to 213.55 MPa whereas the corresponding value of E is 4.77 GPa.

A previous study demonstrated that irregularity at low levels leads to a reduction in strength, which is caused by the initial instability of the unit cell[48]. The increase of irregularity makes more struts change from vertical or horizontal position to inclined position, which is the possible reason for the reduction of the structural stiffness. Thus, a new stress balance will be established and the compressive strength will tend to be stable as the irregularity exceeds a certain value. Furthermore, pores and cracks will inevitably appear in the as-built specimens during the LPBF process. Cracks, related to the direction of struts, have a significant impact on the compressive strength, which also lead to the fluctuation of the experiment data[49-51].

As mentioned in previous studies[52,53], the natural cancellous bone has a Young's modulus range between 0.1 GPa and 4.5 GPa and an ultimate strength range between 1.5 MPa and 38 MPa. Meanwhile, the cortical bone has a Young's modulus range of 5–23 GPa and an ultimate strength range of 35–283 MPa. In this study, the quasi-static compressive behavior of the as-built specimens is researched. The as-built specimens present a satisfying

Figure 14. Bionic bone scaffolds for femoral defect site.

mechanical performance. The apparent elastic modulus ranges from 1.50 GPa to 7.12 GPa, which is in conformance to the required level of natural bone. Besides, the ultimate strength ranges between 38.55 MPa and 268.03 MPa, showing a more excellent stress resistance ability similar to cortical bone level. Compared to the previous studies, the bionic bone scaffolds proposed in this work present a better mechanical continuity with a more reasonable gradient match in elastic modulus and structural strength. Therefore, it can be foreseen that this bionic bone scaffold will help to form a maximum degree of continuous mechanical conduction with the surrounding host bone, further reducing the possibility of the stress shielding. In addition, as shown in Figure 14, this approach is adaptable to models with complex macrostructure, providing more possibilities for engineering application of graded porous biomaterials.

4. Conclusion and future work

In this paper, a sub-regional design methodology of the bionic bone scaffolds, based on the macrostructural topology, was innovatively proposed. The relationship between design parameters and characteristic parameters was fully discussed, indicating that this bionic bone scaffold is highly controllable. The as-designed models were fabricated by the LPBF process using the Ti-6Al-4V powder. The results of FEA and the quasi-static compression tests proved the effectiveness in

practical application. The main results are summarized as follows:

(i) This approach enabled us to carry out accurate and controllable gradient design according to the macrostructural topology, and to implement the graded distribution of the characteristic parameters.

(ii) The combined probability sphere model, proposed in this paper, realized a graded and random distribution of the Voronoi nucleating points, and provided greater freedom in the morphology of the bionic bone scaffolds within a controllable range, further improving the geometric and mechanical continuity at the junction of the two sub-regions.

(iii) The distance-to-scale coefficient mapping model, proposed in this paper, provided the guideline for the graded design of the porous biomaterials in sub-region B, where the specific surface area and the mechanical properties were greatly improved with the differentiated design of C^{face} and C^{cell}, reducing the possibility that fragile struts, far from sub-region A, will fracture first.

(iv) The FEA results showed that randomness and a_1 value have negligible effect on the compressive property and the porosity of as-designed models, proving a high repeatability of tests. Meanwhile, the value of a_2 is considered to have a great influence on the compressive property, proving that the relative density of porous biomaterials in sub-region A is closely related to the structural strength.

(v) The results of quasi-static compression tests demonstrate that ε, C_1, and C_2 affect the compressive behavior of the as-built specimens, proving that C^{cell} of the porous biomaterials in sub-region A has a dominant influence on the compressive property. Meanwhile, the bionic bone scaffolds, proposed in this work, present a satisfying mechanical performance where the apparent elastic modulus and ultimate strength ranges are 1.50–7.12 GPa and 38.55–268.03 MPa, respectively. It can be concluded that the as-built specimens have the same stiffness level of the cancellous bone but with a better stress resistance ability, similar to that of the cortical bone. Significantly, the apparent elastic modulus can be tailored conveniently by adjusting the scale coefficient.

As for the future works, the properties of the bionic bone scaffolds will be further investigated. In addition, research on the bionic bone scaffolds with complex macroscopic models and loading conditions has become the principal work for the next stage. Besides, we also plan to set different topological objectives for the macrostructure to realize multifunctionality of the scaffolds. It is expected that this research can provide some insights into the FGPMs design.

Acknowledgments

Funding

Conflict of interest

The authors declare that they have no known competing financial interests or personal relationships that could have appeared to influence the work reported in this paper.

Author contributions

Conceptualization: Yangdong He, Lida Shen
Investigation: Changjiang Wang, Lin Wang, Deqiao Xie, Chen Jiao, Hong Wang
Methodology: Yangdong He, Long Chao, Huixin Liang
Resources: Jianfeng Zhao, Lida Shen, Huixin Liang, Guofeng Wu
Writing – original draft: Yangdong He
Writing – review & editing: Yangdong He, Long Chao, Huixin Liang, Lida Shen

Ethics approval and consent to participate

Not applicable.

Consent for publication

Not applicable.

Availability of data

The datasets used and analyzed during the present study can be obtained from the corresponding author on request.

References

1. Pina S, Oliveira JM, Reis RL, 2015, Natural-based nanocomposites for bone tissue engineering and regenerative medicine: A review. *Adv Mater*, 27:1143–1169.

https://doi.org/10.1002/adma.201403354

2. Geetha M, Singh AK, Asokamani R, *et al.*, 2009, Ti based biomaterials, the ultimate choice for orthopaedic implants—A review. *Prog Mater Sci*, 54:397–425.

https://doi.org/10.1016/j.pmatsci.2008.06.004

3. Choi K, Kuhn JL, Ciarelli MJ, *et al.*, 1990, The elastic-moduli of human subchondral, trabecular, and cortical bone tissue and the size-dependency of cortical bone modulus. *J Biomech*, 23:1103–1113.

https://doi.org/10.1016/0021-9290(90)90003-l

4. Melancon D, Bagheri ZS, Johnston RB, *et al.*, 2017, Mechanical characterization of structurally porous biomaterials built via additive manufacturing: experiments, predictive models, and design maps for load-bearing bone replacement implants. *Acta Biomater*, 63:350–368.

https://doi.org/10.1016/j.actbio.2017.09.013

5. Kantaros A, Chatzidai N, Karalekas D, 2016, 3D printing-assisted design of scaffold structures. *Int J Adv Manuf Technol*, 82:559–571.

https://doi.org/10.1007/s00170-015-7386-6

6. Tshephe TS, Akinwamide SO, Olevsky E, *et al.*, 2022, Additive manufacturing of titanium-based alloys—A review of methods, properties, challenges, and prospects. *Heliyon*, 8:20.

https://doi.org/10.1016/j.heliyon.2022.e09041

7. Zhao D, Huang Y, Ao Y, *et al.*, 2018, Effect of pore geometry on the fatigue properties and cell affinity of porous titanium scaffolds fabricated by selective laser melting. *J Mech Behav Biomed Mater*, 88:478–487.

https://doi.org/10.1016/j.jmbbm.2018.08.048

8. Yan X, Li Q, Yin S, *et al.*, 2019, Mechanical and in vitro study of an isotropic Ti6Al4V lattice structure fabricated using selective laser melting, *J Alloy Compd*, 782:209–223.

https://doi.org/10.1016/j.jallcom.2018.12.220

9. Gomez S, Vlad MD, Lopez J, *et al.*, 2016, Design and properties of 3D scaffolds for bone tissue engineering, *Acta Biomater*, 42:341–350.

https://doi.org/10.1016/j.actbio.2016.06.032

10. Rumpler M, Woesz A, Dunlop JWC, *et al.*, 2008, The effect of geometry on three-dimensional tissue growth, *J R Soc Interface*, 5:1173–1180.

https://doi.org/10.1098/rsif.2008.0064

11. Biemond JE, Aquarius R, Verdonschot N, *et al.*, 2011, Frictional and bone ingrowth properties of engineered surface topographies produced by electron beam technology. *Arch Orthop Trauma Surg*, 131:711–718.

https://doi.org/10.1007/s00402-010-1218-9

12. Wang G, Shen L, Zhao J, *et al.*, 2018, Design and compressive behavior of controllable irregular porous scaffolds: Based on Voronoi-tessellation and for additive manufacturing. *ACS Biomater Sci Eng*, 4:719–727.

https://doi.org/10.1021/acsbiomaterials.7b00916

13. Du Y, Liang H, Xie D, *et al.*, 2020, Design and statistical analysis of irregular porous scaffolds for orthopedic reconstruction based on Voronoi tessellation and fabricated via selective laser melting (SLM). *Mater Chem Phys*, 239:121968.

https://doi.org/10.1016/j.matchemphys.2019.121968

14. Van Bael S, Chai YC, Truscello S, *et al.*, 2012, The effect of pore geometry on the in vitro biological behavior of human periosteum-derived cells seeded on selective laser-melted Ti6Al4V bone scaffolds. *Acta Biomater*, 8:2824–2834.

https://doi.org/10.1016/j.actbio.2012.04.001

15. Gongyi H, 2007, Characteristics of osteoporosis-related fracture and clinical study. *Basic Clin Med*, 27:1088–1092.

16. Barbaros I, Yang YM, Safaei B, *et al.*, 2022, State-of-the-art review of fabrication, application, and mechanical properties of functionally graded porous nanocomposite materials. *Nanotechnol Rev*, 11:321–371.

https://doi.org/10.1515/ntrev-2022-0017

17. Liu B, Chen H, Cao W, 2019, A novel method for tailoring elasticity distributions of functionally graded porous materials. *Int J Mech Sci*, 157–158:457–470.

https://doi.org/10.1016/j.ijmecsci.2019.05.002

18. George SM, Nayak C, Singh I, *et al.*, 2022, Multifunctional hydroxyapatite composites for orthopedic applications: A review. *ACS Biomater Sci Eng*, 8:3162–3186.

https://doi.org/10.1021/acsbiomaterials.2c00140

19. Deering J, Dowling KI, DiCecco LA, *et al.*, 2021, Selective Voronoi tessellation as a method to design anisotropic and biomimetic implants. *J Mech Behav Biomed Mater*, 116:104361.

https://doi.org/10.1016/j.jmbbm.2021.104361

20. Liu B, Cao W, Zhang L, *et al.*, 2021, A design method of Voronoi porous structures with graded relative elasticity distribution for functionally gradient porous materials. *Int J Mech Mater Des*, 17:863–883.

https://doi.org/10.1007/s10999-021-09558-6

21. Davoodi E, Montazerian H, Mirhakimi AS, *et al.*, 2022, Additively manufactured metallic biomaterials, *Bioact Mater*, 15:214–249.

https://doi.org/10.1016/j.bioactmat.2021.12.027

22. Zhou J, Xia L, Huang K, 2022, Design-oriented topology optimization of structures. *J Ship Mech*, 26:538–546.

23. Xu FX, Zhang X, Zhang H, 2018, A review on functionally graded structures and materials for energy absorption. *Eng Struct*, 171:309–325.

https://doi.org/10.1016/j.engstruct.2018.05.094

24. Li H, Luo Z, Gao L, *et al.*, 2018, Topology optimization for concurrent design of structures with multi-patch microstructures by level sets. *Comput Meth Appl Mech Eng*, 331:536–561.

https://doi.org/10.1016/j.cma.2017.11.033

25. Terriault P, Brailovski V, 2018, Modeling and simulation of large, conformal, porosity-graded and lightweight lattice structures made by additive manufacturing. *Finite Elem Anal Des*, 138:1–11.

https://doi.org/10.1016/j.finel.2017.09.005

26. Radman A, Huang X, Xie YM, 2012, Topology optimization of functionally graded cellular materials. *J Mater Sci*, 48:1503–1510.

https://doi.org/10.1007/s10853-012-6905-1

27. Alzahrani M, Choi SK, Rosen DW, 2015, Design of truss-like cellular structures using relative density mapping method. *Mater Des*, 85:349–360.

https://doi.org/10.1016/j.matdes.2015.06.180

28. Zhao F, 2018, Variable density cellular structure design method base on local relative density mapping. *J Mech Eng*, 54:121–8.

https://doi.org/10.3901/jme.2018.19.121

29. Wang C, Gu X, Zhu J, *et al.*, 2020, Concurrent design of hierarchical structures with three-dimensional parameterized lattice microstructures for additive manufacturing. *Struct Multidiscip O*, 61:869–894.

https://doi.org/10.1007/s00158-019-02408-2

30. Xia L, Xia Q, Huang XD, *et al.*, 2018, Bi-directional evolutionary structural optimization on advanced structures and materials: A comprehensive review. *Arch Comput Method Eng*, 25:437–478.

https://doi.org/10.1007/s11831-016-9203-2

31. Lee TU, Xie YM, 2022, Optimizing load locations and directions in structural design. *Finite Elem Anal Des*, 209:8.

https://doi.org/10.1016/j.finel.2022.103811

32 Bi MH, Tran P, Xia LW, *et al.*, 2022, Topology optimization for 3D concrete printing with various manufacturing constraints. *Addit Manuf*, 57:15.

https://doi.org/10.1016/j.addma.2022.102982

33. Han YS, Xu B, Duan ZY, *et al.*, 2022, Stress-based topology optimization of continuum structures for the elastic contact problems with friction. *Struct Multidiscip O*, 65:22.

https://doi.org/10.1007/s00158-022-03169-1

34. Han YS, Xu B, Duan ZY, *et al.*, 2022, Stress-based multi-material structural topology optimization considering graded interfaces. *Comput Meth Appl Mech Eng*, 391:31.

https://doi.org/10.1016/j.cma.2022.114602

35. Zhu L, Liang H, Lv F, *et al.*, 2021, Design and compressive fatigue properties of irregular porous scaffolds for orthopedics fabricated using selective laser melting, *ACS Biomater Sci Eng*, 7:1663–1672.

https://doi.org/10.1021/acsbiomaterials.0c01392

36. Liang H, Yang Y, Xie D, *et al.*, 2019, Trabecular-like Ti-6Al-4V scaffolds for orthopedic: fabrication by selective laser melting and in vitro biocompatibility. *J Mater Sci Technol*, 35:1284–1297.

https://doi.org/10.1016/j.jmst.2019.01.012

37. Li Y, 2014, *Deformable Geometry Design with Controlled Mechanical Property Based on 3D Printing*, University of Southern California, 162.

38. Radman A, 2021, Combination of BESO and harmony search for topology optimization of microstructures for materials. *Appl Math Model*, 90:650–661.

https://doi.org/10.1016/j.apm.2020.09.024

39. Hutmacher DW, 2000, Scaffolds in tissue engineering bone and cartilage. *Biomaterials*, 21:2529–2543.

https://doi.org/10.1016/s0142-9612(00)00121-6

40. Yan QY, Cheng Y, Wang RR, *et al.*, 2022, Recent advances in 3D porous MXenes: Structures, properties and applications. *J Phys D-Appl Phys*, 55:15.

https://doi.org/10.1088/1361-6463/ac2db2

41. Prananingrum W, Naito Y, Galli S, *et al.*, 2016, Bone ingrowth of various porous titanium scaffolds produced by a moldless and space holder technique: an in vivo study in rabbits. *Biomed Mater*, 11:8.

https://doi.org/10.1088/1748-6041/11/1/015012

42. Babaie E, Bhaduri SB, 2018, Fabrication aspects of porous biomaterials in orthopedic applications: A review, *ACS Biomater Sci Eng*, 4:1–39.

https://doi.org/10.1021/acsbiomaterials.7b00615

43. Zheng YH, Han Q, Wang JC, *et al.*, 2020, Promotion of osseointegration between implant and bone interface by titanium alloy porous scaffolds prepared by 3D printing. *ACS Biomater Sci Eng*, 6:5181–5190.

https://doi.org/10.1021/acsbiomaterials.0c00662

44. Zhang S, 2016, Foam metal research and application progress. *Powder Metall Technol*, 34:222–227.

45. Qiu SW, Zhang XN, Hao QX, *et al.*, 2015, Research progress on simulation modeling of metal foams. *Rare Metal Mat Eng*, 44:2670–2676.

46. Gibson LJ, 2003, Cellular solids. *MRS Bull*, 28:270–271.

https://doi.org/10.1557/mrs2003.79

47. Gibson LJ, Ashby MF, 1997, *Cellular Solids: Structure and Properties*, Cambridge University Press, Cambridge, 387–428.

48. Mullen L, Stamp RC, Brooks WK, *et al.*, 2009, Selective laser melting: A regular unit cell approach for the manufacture of porous, titanium, bone in-growth constructs, suitable for orthopedic applications. *J Biomed Mater Res Part B*, 89B:325–334.

https://doi.org/10.1002/jbm.b.31219

49. Craeghs T, Clijsters S, Yasa E, *et al.*, 2011, Determination of geometrical factors in Layerwise laser melting using optical process monitoring. *Opt Lasers Eng*, 49:1440–1446.

https://doi.org/10.1016/j.optlaseng.2011.06.016

50. Wauthle R, Vrancken B, Beynaerts B, *et al.*, 2015, Effects of build orientation and heat treatment on the microstructure and mechanical properties of selective laser melted Ti6Al4V lattice structures. *Addit Manuf*, 5:77–84.

https://doi.org/10.1016/j.addma.2014.12.008

51. Popovich A, Sufiiarov V, Borisov E, *et al.*, 2015, Microstructure and mechanical properties of Ti-6Al-4V manufactured by SLM. *Key Eng Mater (Switzerland)*, 651–653: 677–682.

https://doi.org/10.4028/www.scientific.net/KEM.651-653.677

52. Sevilla P, Aparicio C, Planell JA, *et al.*, 2007, Comparison of the mechanical properties between tantalum and nickel-titanium foams implant materials for bone ingrowth applications. *J Alloy Compd*, 439:67–73.

https://doi.org/10.1016/j.jallcom.2006.08.069

53. Morgan EF, Bayraktar HH, Keaveny TM, 2003, Trabecular bone modulus-density relationships depend on anatomic site. *J Biomech*, 36:897–904.

https://doi.org/10.1016/s0021-9290(03)00071-x